Editors' Suggestion | Featured in Physics

Improved Upper Limit on the Neutrino Mass from a Direct Kinematic Method by KATRIN

M. Aker,[1,2] K. Altenmüller,[10,3,4] M. Arenz,[5] M. Babutzka,[6] J. Barrett,[7] S. Bauer,[8] M. Beck,[8,12] A. Beglarian,[9] J. Behrens,[6,1,8] T. Bergmann,[10,3,9] U. Besserer,[1,2] K. Blaum,[11] F. Block,[6] S. Bobien,[2] K. Bokeloh,[8§] J. Bonn,[12,*] B. Bornschein,[1,2] L. Bornschein,[1] H. Bouquet,[9] T. Brunst,[10,3] T. S. Caldwell,[13,14] L. La Cascio,[6] S. Chilingaryan,[9] W. Choi,[6] T. J. Corona,[13,14,7] K. Debowski,[15,6] M. Deffert,[6] M. Descher,[6] P. J. Doe,[16] O. Dragoun,[17] G. Drexlin,[6,1†] J. A. Dunmore,[16] S. Dyba,[8] F. Edzards,[10,3] L. Eisenblätter,[9] K. Eitel,[1] E. Ellinger,[15] R. Engel,[1,6] S. Enomoto,[16] M. Erhard,[6] D. Eversheim,[5] M. Fedkevych,[8] A. Felden,[1] S. Fischer,[1,2] B. Flatt,[12] J. A. Formaggio,[7] F. M. Fränkle,[1,13,14] G. B. Franklin,[18] H. Frankrone,[9] F. Friedel,[6] D. Fuchs,[10,3] A. Fulst,[8] D. Furse,[7] K. Gauda,[8] H. Gemmeke,[9] W. Gil,[1] F. Glück,[1] S. Görhardt,[1] S. Groh,[6] S. Grohmann,[2] R. Grössle,[1,2] R. Gumbsheimer,[1] M. Ha Minh,[10,3] M. Hackenjos,[1,2,6] V. Hannen,[8] F. Harms,[6] J. Hartmann,[9] N. Haußmann,[15] F. Heizmann,[6] K. Helbing,[15] S. Hickford,[1,15] D. Hilk,[6] B. Hillen,[8] D. Hillesheimer,[1,2] D. Hinz,[1] T. Höhn,[1] B. Holzapfel,[2] S. Holzmann,[2] T. Houdy,[10,3] M. A. Howe,[13,14] A. Huber,[6] T. M. James,[2] A. Jansen,[1] A. Kaboth,[7] C. Karl,[10,3] O. Kazachenko,[21] J. Kellerer,[6] N. Kernert,[1] L. Kippenbrock,[16] M. Kleesiek,[6‖] M. Klein,[1,6] C. Köhler,[10,3] L. Köllenberger,[1] A. Kopmann,[9] M. Korzeczek,[6] A. Kosmider,[1] A. Kovalík,[17] B. Krasch,[1,2] M. Kraus,[6] H. Krause,[1] L. Kuckert,[1¶] B. Kuffner,[1] N. Kunka,[9] T. Lasserre,[4,3,10] T. L. Le,[1,2] O. Lebeda,[17] M. Leber,[16] B. Lehnert,[19] J. Letnev,[20] F. Leven,[6] S. Lichter,[1] V. M. Lobashev,[21,*] A. Lokhov,[8,21] M. Machatschek,[6] E. Malcherek,[1] K. Müller,[1] M. Mark,[1] A. Marsteller,[1,2] E. L. Martin,[13,14,16] C. Melzer,[1,2] A. Menshikov,[9] S. Mertens,[10,3,19,1] L. I. Minter,[16**] S. Mirz,[1,2] B. Monreal,[22] P. I. Morales Guzmán,[10,3] K. Müller,[1] U. Naumann,[15] W. Ndeke,[25] H. Neumann,[2] S. Niemes,[1,2] M. Noe,[2] N. S. Oblath,[7] H.-W. Ortjohann,[8] A. Osipowicz,[20] B. Ostrick,[8] E. Otten,[12,*] D. S. Parno,[18,16] D. G. Phillips II,[13,14] P. Plischke,[1] A. Pollithy,[10,3] A. W. P. Poon,[19] J. Pouryamout,[15] M. Prall,[8] F. Priester,[1,2] M. Röllig,[1,2] C. Röttele,[1,6,2] P. C.-O. Ranitzsch,[8] O. Rest,[8] R. Rinderspacher,[1] R. G. H. Robertson,[16] C. Rodenbeck,[8] P. Rohr,[9] Ch. Roll,[25] S. Rupp,[1,2,6] M. Ryšavý,[17] R. Sack,[8] A. Saenz,[25] P. Schäfer,[1,2] L. Schimpf,[6] K. Schlösser,[1] M. Schlösser,[1,2] L. Schlüter,[10,3] H. Schön,[2] K. Schönung,[11,1,2] M. Schrank,[1] B. Schulz,[25] J. Schwarz,[1] H. Seitz-Moskaliuk,[6] W. Seller,[20] V. Sibille,[7] D. Siegmann,[10,3] A. Skasyrskaya,[21] M. Slezák,[10,17] A. Špalek,[17] F. Spanier,[1] M. Steidl,[1] N. Steinbrink,[8] M. Sturm,[1,2] M. Suesser,[2] M. Sun,[16] D. Tcherniakhovski,[9] H. H. Telle,[23] T. Thümmler,[1,8] L. A. Thorne,[18] N. Titov,[21] I. Tkachev,[21] N. Trost,[1] K. Urban,[10,3] D. Vénos,[17] K. Valerius,[1,8] B. A. VanDevender,[16] R. Vianden,[5] A. P. Vizcaya Hernández,[18] B. L. Wall,[16] S. Wüstling,[9] M. Weber,[9] C. Weinheimer,[8‡] C. Weiss,[24] S. Welte,[1,2] J. Wendel,[1,2] K. J. Wierman,[13,14] J. F. Wilkerson,[13,14††] J. Wolf,[6] W. Xu,[7] Y.-R. Yen,[18] M. Zacher,[8] S. Zadorozhny,[21] M. Zbořil,[8,17] and G. Zeller[1,2]

(KATRIN Collaboration)

[1]*Institute for Nuclear Physics (IKP), Karlsruhe Institute of Technology (KIT), Hermann-von-Helmholtz-Platz 1, 76344 Eggenstein-Leopoldshafen, Germany*
[2]*Institute for Technical Physics (ITEP), Karlsruhe Institute of Technology (KIT), Hermann-von-Helmholtz-Platz 1, 76344 Eggenstein-Leopoldshafen, Germany*
[3]*Technische Universität München, James-Franck-Straße 1, 85748 Garching, Germany*
[4]*IRFU (DPhP & APC), CEA, Université Paris-Saclay, 91191 Gif-sur-Yvette, France*
[5]*Helmholtz-Institut für Strahlen- und Kernphysik, Rheinische Friedrich-Wilhelms-Universität Bonn, Nussallee 14-16, 53115 Bonn, Germany*
[6]*Institute of Experimental Particle Physics (ETP), Karlsruhe Institute of Technology (KIT), Wolfgang-Gaede-Straße 1, 76131 Karlsruhe, Germany*
[7]*Laboratory for Nuclear Science, Massachusetts Institute of Technology, 77 Massachusetts Avenue, Cambridge, Massachusetts 02139, USA*
[8]*Institut für Kernphysik, Westfälische Wilhelms-Universität Münster, Wilhelm-Klemm-Straße 9, 48149 Münster, Germany*
[9]*Institute for Data Processing and Electronics (IPE), Karlsruhe Institute of Technology (KIT), Hermann-von-Helmholtz-Platz 1, 76344 Eggenstein-Leopoldshafen, Germany*
[10]*Max-Planck-Institut für Physik, Föhringer Ring 6, 80805 München, Germany*
[11]*Max-Planck-Institut für Kernphysik, Saupfercheckweg 1, 69117 Heidelberg, Germany*
[12]*Institut für Physik, Johannes-Gutenberg-Universität Mainz, 55099 Mainz, Germany*
[13]*Department of Physics and Astronomy, University of North Carolina, Chapel Hill, North Carolina 27599, USA*
[14]*Triangle Universities Nuclear Laboratory, Durham, North Carolina 27708, USA*

[15]Department of Physics, Faculty of Mathematics and Natural Sciences, University of Wuppertal, Gaußstraße 20, 42119 Wuppertal, Germany
[16]Center for Experimental Nuclear Physics and Astrophysics, and Department of Physics, University of Washington, Seattle, Washington 98195, USA
[17]Nuclear Physics Institute of the CAS, v. v. i., CZ-250 68 Řež, Czech Republic
[18]Department of Physics, Carnegie Mellon University, Pittsburgh, Pennsylvania 15213, USA
[19]Institute for Nuclear and Particle Astrophysics and Nuclear Science Division, Lawrence Berkeley National Laboratory, Berkeley, California 94720, USA
[20]University of Applied Sciences (HFD) Fulda, Leipziger Straße 123, 36037 Fulda, Germany
[21]Institute for Nuclear Research of Russian Academy of Sciences, 60th October Anniversary Prospect 7a, 117312 Moscow, Russia
[22]Department of Physics, Case Western Reserve University, Cleveland, Ohio 44106, USA
[23]Departamento de Química Física Aplicada, Universidad Autonoma de Madrid, Campus de Cantoblanco, 28049 Madrid, Spain
[24]Project, Process, and Quality Management (PPQ), Karlsruhe Institute of Technology (KIT), Hermann-von-Helmholtz-Platz 1, 76344 Eggenstein-Leopoldshafen, Germany
[25]Institut für Physik, Humboldt-Universität zu Berlin, Newtonstraße 15, 12489 Berlin, Germany

(Received 18 September 2019; published 25 November 2019)

We report on the neutrino mass measurement result from the first four-week science run of the Karlsruhe Tritium Neutrino experiment KATRIN in spring 2019. Beta-decay electrons from a high-purity gaseous molecular tritium source are energy analyzed by a high-resolution MAC-E filter. A fit of the integrated electron spectrum over a narrow interval around the kinematic end point at 18.57 keV gives an effective neutrino mass square value of $(-1.0^{+0.9}_{-1.1})$ eV^2. From this, we derive an upper limit of 1.1 eV (90% confidence level) on the absolute mass scale of neutrinos. This value coincides with the KATRIN sensitivity. It improves upon previous mass limits from kinematic measurements by almost a factor of 2 and provides model-independent input to cosmological studies of structure formation.

DOI: 10.1103/PhysRevLett.123.221802

Introduction.—The observation of flavor oscillations of atmospheric and solar neutrinos [1,2] as well as oscillation studies at reactors and accelerators unequivocally prove neutrinos to possess nonzero rest masses (e.g., [3]), contradicting the standard model (SM) expectation of them being massless. The absolute values m_i of the neutrino mass states ν_i ($i = 1, 2, 3$), which cannot be probed by oscillations, are of fundamental importance in cosmological studies [4–6] and for particle physics models beyond the SM [7].

Because of the unique role of primordial neutrinos in the formation of large-scale structures in the universe, observations of matter clustering in different epochs of the universe allow one to probe the neutrino mass sum $\Sigma_i m_i$. The current upper limits depend on the selection of data sets included in the analyses and are valid only within the ΛCDM concordance model [6,8]. Another model-dependent method is provided by the search for neutrinoless double beta decay $0\nu\beta\beta$, a process forbidden in the SM due to lepton number violation. It gives access to the effective Majorana neutrino mass (e.g., [9,10]).

A model-independent, direct method for probing the neutrino mass scale in the laboratory is provided by kinematic studies of weak-interaction processes such as β decay of tritium (^{3}H) and electron capture on holmium (^{163}Ho) [11–15]. These investigations yield an incoherent sum of spectra, containing the squares of the neutrino eigenmasses m_i^2 as parameters. Each spectral component is weighted by the absolute square of the corresponding electron-flavor matrix element $|U_{ei}|^2$. In the quasidegenerate regime $m_i > 0.2$ eV, the eigenmasses are the same to better than 3%. The mass measured in β decay or electron capture, often called "$m(\nu_e)$," is the neutrino mass $m_\nu \approx m_i$ in this regime.

Because of its low end point energy ($E_0 = 18.57$ keV) and favorable half-life ($t_{1/2} = 12.32$ yr), the decay of tritium $^3\mathrm{H} \rightarrow {}^3\mathrm{He}^+ + e^- + \bar{\nu}_e$ has been investigated by a large number of experiments looking for the small, characteristic shape distortion of the β spectrum close to E_0 due to m_ν [11,12]. Experimental advances over many decades have steadily increased the sensitivity to the present upper limit of $m_\nu < 2$ eV (95% confidence level, C.L.) [16]. In this Letter, we report on the first neutrino mass result from the Karlsruhe Tritium Neutrino experiment KATRIN [17–20], which is targeted to advance the sensitivity on m_ν by 1 order of magnitude down to 0.2 eV (90% C.L.) after five years.

Experimental setup.—KATRIN combines a windowless gaseous molecular tritium source (WGTS), pioneered by

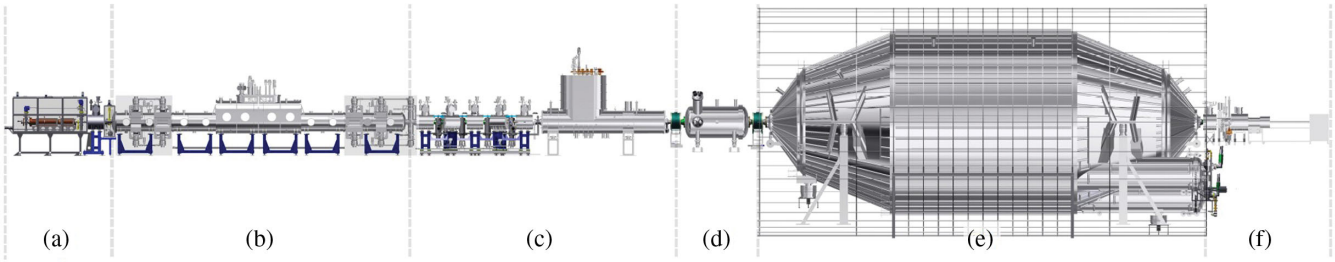

FIG. 1. The major components of the KATRIN beam line consist of (a) the rear section for diagnostics, (b) the windowless gaseous tritium source WGTS, c) the pumping section with the DPS and CPS cryostats, and a tandem setup of two MAC-E-filters: (d) the smaller prespectrometer and (e) the larger main spectrometer with its surrounding air coil system. This system transmits only the highest-energy β decay electrons onto (f) the solid-state detector where they are counted.

the Los Alamos experiment [21], with a spectrometer based on the principle of magnetic adiabatic collimation with electrostatic filtering (MAC-E-filter) [22,23], developed at Mainz and Troitsk [24,25]. These techniques allow the investigation of the end point region of tritium β decay with very high energy resolution, large statistics, and small systematics. KATRIN has been designed and built to refine this direct kinematic method to its ultimate precision level. To improve the sensitivity on m_ν by 1 order of magnitude calls for an increase in statistics and a reduction of systematic uncertainties by 2 orders of magnitude, as the observable in kinematic studies is the neutrino mass square, m_ν^2.

Figure 1 gives an overview of the 70 m long experimental setup located at the Karlsruhe Institute of Technology. The source-related components in contact with tritium, the rear section (RS) (a), the WGTS cryostat (b), as well as the differential (DPS) and cryogenic (CPS) pumping sections (c) are integrated into the extensive infrastructure of Tritium Laboratory Karlsruhe to enable a closed cycle of tritium [26]. High-purity tritium gas from a pressure-controlled buffer vessel is continuously injected at 30 K into the WGTS at the midpoint of its 90 mm diameter, 10 m long stainless steel beam tube. The gas then diffuses to both ends where it is pumped out by a series of turbomolecular pumps (TMPs) in the DPS, yielding the nominal column density $\rho d_{\mathrm{nom}} = 5 \times 10^{17}$ molecules cm^{-2}. In combination with the CPS, housing a large-capacity cryotrap operated at around 3 K, the flow rate of tritium into the following spectrometer and detector section [Figs. 1(d)–1(f)] downstream is negligible, well below the 14 orders of magnitude of flow reduction required to eliminate source-related background by neutral tritium gas [17].

The source magnetic field (section b) in Fig. 1, $B_{\mathrm{WGTS}} = 2.52$ T) as well as other superconducting solenoids [section (c) in Fig. 1] [27] adiabatically guide primary β-decay electrons, secondary electrons, and ions to the spectrometers. A series of blocking and dipole electrodes eliminates ions by an $\vec{E} \times \vec{B}$ drift to the beam tube, so that they cannot generate background in the spectrometer section [19].

High-precision electron spectroscopy is achieved by the MAC-E-filter technique, where electrons of charge q are guided by the magnetic field, collimated by its gradient and filtered by an electrostatic barrier, the retarding potential energy qU. The resulting high-pass filter transmits only electrons with enough energy to overcome the barrier qU and allows the scanning of the tritium β-decay spectrum in an integral mode.

The tandem configuration of MAC-E-filters performs a two-step filter process: first, the smaller prespectrometer is operated at fixed high voltage (HV) of -10.4 kV in this work to act as a prefilter to reject electrons that carry no information on m_ν. In a second step, a variable qU is applied to the main spectrometer for precision filtering of β-decay electrons close to E_0. Its huge size guarantees fully adiabatic motion to the central "analyzing plane," where the minimum magnetic field B_{min} and the maximum retarding energy qU coincide for the filtering process to occur. Elevating the two spectrometers to a negative HV forms a strong Penning trap which can give rise to background [28,29]. This is avoided by operating both at an ultrahigh vacuum (UHV) regime of 10^{-11} mbar using nonevaporable getter (NEG) pumps and TMPs [30].

A defining property of a MAC-E-filter is $\Delta E/E$, the filter width at energy E, which is given by the ratio $B_{\mathrm{min}}/B_{\mathrm{max}}$ of the minimum to maximum magnetic field in nonrelativistic approximation. The present ratio (0.63 mT/4.24 T) is equivalent to $\Delta E = 2.8$ eV at E_0. This value constrains the size V_{ft} of the flux tube around B_{min} and, consequently, the overall background rate, which is proportional to V_{ft} to the first order. A large air coil system of 12.6 m diameter [31] is used to adjust B_{min} and V_{ft}. After the potential of the spectrometer vessel is elevated, an offset of up to -200 V can be applied to the wire electrode system mounted on the inner surface of the vessel to define qU.

Electrons transmitted through the spectrometers are finally counted in a radially and azimuthally segmented monolithic silicon detector array with 148 pixels [32] as a function of qU. To optimize the signal-to-background ratio, transmitted electrons are postaccelerated by a potential of $+10$ kV before they impinge on the detector.

Commissioning measurements.—Over the past years, we have commissioned the entire setup by a series of dedicated long-term measurements [19,26,27,33] which have demonstrated that all specifications [18] are met, or even surpassed by up to 1 order of magnitude, except for the background rate R_{bg}.

A major benchmark is to operate the source at ρd_{nom} at a stability level of 10^{-3}/h so that variations of the column density ρd can be neglected. This calls for a stable gas injection rate via capillaries [26] and a constant beam-tube temperature. For the latter, a stability level of better than 10^{-3}/h has been achieved by a two-phase beam-tube cooling system at 30 (100) K using neon (argon) as a cooling fluid [34]. In mid-2018, measurements at 1% DT concentration within a 99% D_2 carrier gas at ρd_{nom} have verified the required level of source stability [35]. This "first tritium" campaign has allowed us to collect the first integral electron spectra which agree well with the model expectation.

In this spectral comparison, the response function $f(E-qU)$ [20] plays a fundamental role [see Eq. (1)], as it converts the theoretical β spectrum into the experimental spectrum. It describes the probability of transmission of an electron with initial energy E as a function of its surplus energy $E-qU$. For an ensemble, it depends on the angular spread of electrons and the amount of neutral gas they pass in the source, where they can undergo inelastic scattering processes with a total cross section σ (3.64×10^{-18} cm^2 at 18.57 keV, adopted from [36]).

We measure $f(E-qU)$ using monoenergetic electrons with a small angular spread produced in a dedicated photoelectron source (e gun) [37] located at the RS. These electrons span a 50 eV wide range of surplus energies $E-qU$ and pass through the integral column density ρd of the source. This allows us to measure the characteristics of single ($s=1$) and multiple ($s=2,3,\ldots$) inelastic scattering in T_2. In Fig. 2 (top), we display the measured response $f(E-qU)$ for a narrow-angle photoelectron source as well as the calculated response $f_{\mathrm{calc}}(E-qU)$ for isotropically emitted β-decay electrons for the normal integrating MAC-E mode for $\rho d\approx\rho d_{\mathrm{nom}}$. The sharp rise with the filter width ΔE to a plateau extending up to 11 eV results from "no loss" (energy loss $\delta E=0$) e-gun electrons, which leave the source without scattering ($s=0$) with a probability $\exp(-\rho d\cdot\sigma)$. At larger $E-qU$, s-fold scattering ($s=1$, 2, 3) is visible. In Fig. 2 (bottom), the differential data from the MAC-E-TOF mode [38] are shown, where the electron time of flight (TOF) is recorded. This allows us to even better assess the s-fold inelastic scattering and to obtain the energy-loss function of electrons $\varepsilon(\delta E)$ by a deconvolution with the no loss peak at $\delta E=E-qU=0$.

As the background rate R_{bg} exceeds its design goal of 0.01 counts per second (cps), we have studied the nature and origin of background processes so as to implement

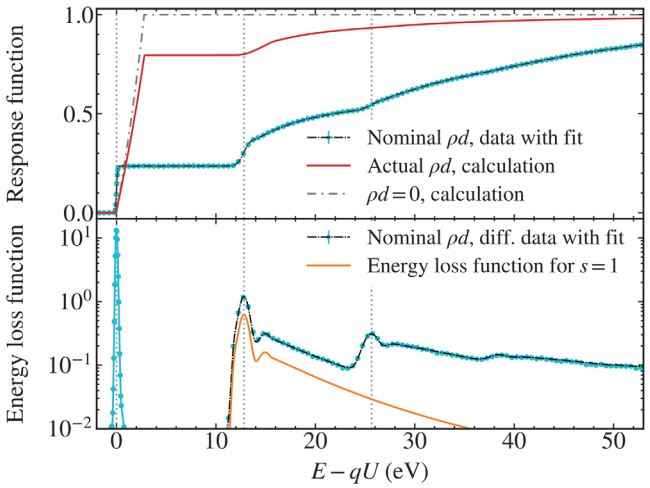

FIG. 2. (top) Measured and calculated response functions $f(E-qU)$ for electron surplus energies $E-qU$ at different ρd values of T_2. Measured $f(E-qU)$ for a narrow-angle photoelectron source close to ρd_{nom} and fit (cyan line); and calculated $f_{\mathrm{calc}}(E-qU)$ for isotropically emitted β decay electrons up to θ_{max} at ρd_{exp} (1.11×10^{17} cm^{-2}), the set point of our scans (red line), and in the limit of vanishing $\rho d=0$ (grey, dashed-dotted line). (bottom) Differential distributions of energy losses δE from the MAC-E-TOF mode after a selection 35 μs $\leq$ TOF $\leq$ 50 μs at $\rho d\approx\rho d_{\mathrm{nom}}$ and fit (cyan line). The "no loss" peak at $\delta E=E-qU=0$ is followed by peaks with $s=2$ ($s=3$) scattering at twice (triple) the δE value of $s=1$. The energy loss function $\varepsilon(\delta E)$ for $s=1$ is obtained by deconvolution (orange line).

mitigation measures. Up to now, source-related backgrounds have not been observed, so that spectrometer-related processes [39] dominate R_{bg} apart from a small detector-related contribution [32]. Electrons generated at the spectrometer surface by cosmic muons and environmental gamma rays are inhibited from entering the inner flux tube by magnetic and electric barriers [40,41]. Thus, R_{bg} originates from excited or unstable neutral atoms which can propagate freely in the UHV environment. Accordingly, R_{bg} is observed to have an almost constant rate per unit volume in the flux tube.

Detailed investigations of the background behavior [39,42] revealed that a significant part of R_{bg} is due to Rydberg atoms sputtered off the inner spectrometer surfaces by ^{206}Pb-recoil ions following α decays of ^{210}Po. These processes follow the decay chain of the long-lived ^{222}Rn progeny ^{210}Pb, which was surface-implanted from ambient air (activity $\approx$1 Bq/m^2) during the construction phase. A small fraction of these Rydberg states is ionized by blackbody radiation when propagating over the magnetic flux tube. The resulting sub-eV scale electrons are accelerated to qU by the MAC-E-filter and form a Poisson component to R_{bg}.

The other part of background events stems from α decays of single ^{219}Rn atoms ($t_{1/2}=3.96$ s) emanating from the

NEG pumps located in two of the three pump ports of the main spectrometer which release a large number of electrons up to the keV scale in the flux tube, where they are stored due to its magnetic bottle characteristics. By scattering off residual gas, the stored electrons subsequently produce secondary background electrons. This process continues until the stored electron is cooled off to an energy of a few eV when it can escape and also contribute itself to R_{bg} at qU. Owing to its origin from a small number of ^{219}Rn decays, this background results in extended time periods where the background level is enhanced yielding a small non-Poissonian component [43]. Liquid-nitrogen cooled copper baffles at the inlet of the NEG pumps act as a countermeasure [44]. The coverage of the inner surface of the main spectrometer with a monolayer of H_2O, originating from an imperfect bake out of the prespectrometer, has led to the formation of a thin layer of H_2O covering the baffle surface. Therefore, the retention of ^{219}Rn in this work is hampered such that R_{bg} retains a small non-Poissonian component.

Measurements of the tritium β spectrum.—In the following, we report on our first high-purity tritium campaign from April 10 to May 13, 2019 which demonstrates the functionality of all system components and of the extensive tritium infrastructure at large source activity (2.45×10^{10} Bq) and tritium throughput (4.9 g/day). As a result of radiochemical reactions of T_2 with the previously unexposed inner metal surface of the injection capillary, we observe drifts in the source column density. To limit these drifts to a level of $\pm 2 \times 10^{-2}$ over our campaign, we keep the column density at an average value of $\rho d_{\mathrm{exp}} = 1.11 \times 10^{17}$ molecules cm^{-2}, which is about a factor of 5 smaller than ρd_{nom}.

At this setting, the smaller value of $\rho d_{\mathrm{exp}} \cdot \sigma$ (0.404) reduces the amount of inelastic scattering of electrons off neutral gas, see Fig. 2. The relative fractions of the six hydrogen isotopologues injected into the source are continuously monitored by laser-Raman spectroscopy with 10^{-3} precision [45]. The average isotopic tritium purity ε_T (0.976) of our analyzed data sample is derived from the composition of the tritiated species T_2 (0.953), HT (0.035), and DT (0.011), with inactive species (D_2, HD, and H_2) being present only in trace amounts.

Because of the large number of β decay s and ionization processes, a cold magnetized plasma of electrons (meV to keV scale) and ions (meV scale) is formed which interacts with the neutral gas. The strong solenoidal field B_{WGTS} and the resulting large longitudinal conductance of the plasma allow the coupling of its potential to the surface of the rear wall (RW) located at the RS and, thus, to control the starting energies of β-decay electrons over the volume [46]. Biasing the gold-plated RW disk with small areal variation of the work function to −0.15 V relative to the grounded beam tube gives a very good radial homogeneity of the source potential. This is verified during initial tritium scans with fits of E_0 over detector pixel rings, which do not show a significant radial variation.

TABLE I. 1σ systematic uncertainties (σ_{syst}) for m_ν^2 in eV^2, averaged over positive and negative errors, using the method of MC propagation.

Effect	Relative uncertainty	$\sigma(m_\nu^2)$ in eV^2
Source properties		
$\rho d \cdot \sigma$	0.85%	0.05
Energy loss $\varepsilon(\delta\mathrm{E})$	$\mathcal{O}(1\%)$	Negligible
Beamline		0.05
B_{WGTS}	2.5%	
B_{min}	1%	
B_{max}	0.2%	
Final state distribution	$\mathcal{O}(1\%)$	0.02
Fluctuations in scan k		0.05
HV stacking	2 ppm	
ρd variation	0.8%	
Isotopologue fractions	0.2%	
Background		
Background slope	1.7%/keV	0.07
Non-Poisson background	6.4%	0.30
Total syst. uncertainty		0.32

Additional information on plasma effects is provided by comparing the line shape and position of quasimonoenergetic conversion electrons (L_3-32) from $^{83\mathrm{m}}$Kr runs in T_2 to $^{83\mathrm{m}}$Kr runs without the carrier gas at 100 K [47]. We do not identify sizeable shifts (< 0.04 eV) or broadening (< 0.08 eV) of lines so that the contribution of plasma effects at ρd_{exp} to the systematic error budget in Table I can be neglected.

The integral tritium β-decay spectrum is scanned repeatedly in a range from $[E_0 - 90\ \mathrm{eV}, E_0 + 50\ \mathrm{eV}]$ by applying a set of nonequidistant HV settings to the inner electrode system. Each scan over this range takes a net time of about 2 h and is performed in alternating upward and downward directions to compensate for any time-dependent drift of the system to first order. At each HV set point, the transmitted electrons are counted over time intervals varying from 17 to 576 s with typical values of ∼300 s for points close to E_0. When setting a new HV value, we make use of a custom-made postregulation system for voltage stabilization and elimination of high-frequency noise. At the same time, a custom-made HV divider [48] continuously monitors the retarding voltage with ppm precision.

To limit the influence of systematic uncertainties for this Letter, we analyze a scan range covering the region of 40 eV below E_0 (22 HV set points) and 50 eV above (5 HV set points). The nonuniform measuring time distribution in this interval is shown in Fig. 3(c). It maximizes the sensitivity for m_ν^2 by focusing on the narrow region below E_0, where the imprint of the neutrino mass on the spectrum is most pronounced [20]. Shorter time intervals with a set

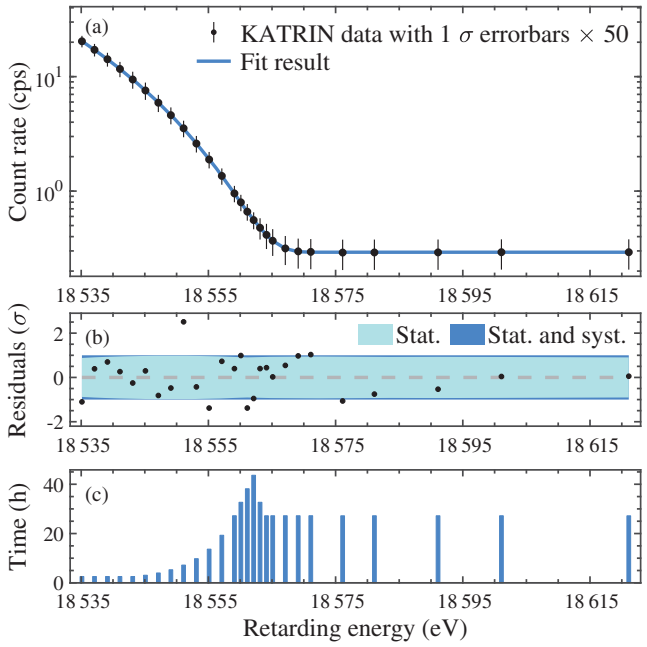

FIG. 3. (a) Spectrum of electrons $R(\langle qU\rangle)$ over a 90 eV-wide interval from all 274 tritium scans and best-fit model $R_{\mathrm{calc}}(\langle qU\rangle)$ (line). The integral β decay spectrum extends up to E_0 on top of a flat background R_{bg}. Experimental data are stacked at the average value $\langle qU\rangle_l$ of each HV set point and are displayed with 1σ statistical uncertainties enlarged by a factor of 50. (b) Residuals of $R(\langle qU\rangle)$ relative to the 1σ uncertainty band of the best fit model. (c) Integral measurement time distribution of all 27 HV set points.

point 200 V below E_0 are interspersed to monitor the source activity, in addition to other measures [49].

Data analysis.—For each tritium scan with its 27 HV set points, we apply quality cuts to relevant slow-control parameters to select a data set with stable run conditions. This results in 274 scans with an overall scanning time of 521.7 h. We also define a list of 117 detector pixels (out of 148), which excludes those pixels that are noisy or shadowed by beam line instrumentation in the β-electron path along the magnetic flux tube. For the digitized, calibrated and pile-up-corrected detector spectra, a broad region of interest (ROI) between 14 and 32 keV is defined. The ROI takes into account the detector energy resolution and its elevated potential (+10 kV) and allows us to include a large fraction of electrons backscattered at the detector in the narrow scan region close to E_0 resulting in a negligible contribution to the systematic uncertainty budget [32].

The long-term stability of the scanning process is verified by fits to single scans to extract their effective β-decay end points. The 274 fit values show no time-dependent behavior and follow a Gaussian distribution ($\sigma = 0.25$ eV) around a mean value of $E_0 = 18\,573.7$ eV. In view of this and the very good overall stability of the slow-control parameters for our data set, we merge the data of all 274 scans over all 117 pixels into one single 90-eV-wide spectrum, which is displayed in Fig. 3(a) in units of cps.

The underlying process corresponds to the "stacking" of events at the mean HV set points $\langle qU\rangle_l$ ($l = 1$–27). The small Gaussian spread (rms = 34 mV) of the actual HV value $qU_{l,k}$ during a scan k relative to $\langle qU\rangle_l$, the average of all scans, is a minor systematic effect which is accounted for in the analysis. The resulting stacked integral spectrum, $\mathrm{R}(\langle qU\rangle)$, comprises 2.03×10^6 events, with 1.48×10^6 β-decay electrons below E_0 and a flat background ensemble of 0.55×10^6 events in the 90 eV scan interval. This high-statistics data set allows us to show 1σ error bars enlarged by a factor of 50 in Fig. 3.

The experimental spectrum is well described by our detailed model of the KATRIN response to β-decay electrons and background. It contains four free parameters: the signal amplitude A_s, the effective β-decay end point E_0, the background rate R_{bg}, and the neutrino mass square m_ν^2. We leave E_0 and A_s unconstrained, which is equivalent to a "shape-only" fit. The goodness-of-fit is illustrated in Fig. 3(b) from the scatter of residuals around the error band of the model.

The four-parameter fit procedure over the averaged HV set points $\langle qU\rangle_l$ compares the experimental spectrum $\mathrm{R}(\langle qU\rangle)$ to the model $R_{\mathrm{calc}}(\langle qU\rangle)$. The latter is the convolution of the differential β-electron spectrum $R_\beta(E)$ with the calculated response function $f_{\mathrm{calc}}(E - \langle qU\rangle)$, with an added energy-independent background rate R_{bg}

$$R_{\mathrm{calc}}(\langle qU\rangle) = A_s N_T \int R_\beta(E) f_{\mathrm{calc}}(E - \langle qU\rangle) dE + R_{\mathrm{bg}}. \tag{1}$$

Here, N_T denotes the calculated number of tritium atoms in the source multiplied with the accepted solid angle of the setup $\Delta\Omega/4\pi = (1 - \cos\theta_{\mathrm{max}})/2$ and the detector efficiency [$\theta_{\mathrm{max}} = \arcsin\sqrt{(B_{\mathrm{WGTS}}/B_{\mathrm{max}})} = 50.4°$], its uncertainty is absorbed by the fit parameter A_s.

The electron spectrum $R_\beta(E)$ from the superallowed β decay of molecular tritium is calculated using Fermi's Golden Rule

$$\begin{aligned} R_\beta(E) = {} & \frac{G_F^2 \cdot \cos^2\Theta_{\mathrm{C}}}{2\pi^3} |M_{\mathrm{nucl}}^2| F(E, Z') \\ & \times (E + m_{\mathrm{e}}) \sqrt{(E + m_{\mathrm{e}})^2 - m_{\mathrm{e}}^2} \\ & \times \sum_{\mathrm{j}} \zeta_j \varepsilon_j \sqrt{\varepsilon_j^2 - m_\nu^2}\, \Theta(\varepsilon_j - m_\nu), \end{aligned} \tag{2}$$

with the square of the energy-independent nuclear matrix element $|M_{\mathrm{nucl}}^2|$, the Fermi constant G_F, the Cabibbo angle Θ_C, the electron mass m_e, the Fermi function $F(E, Z' = 2)$, and the neutrino energy $\varepsilon_j = E_0 - E - V_j$. In addition, our

calculations incorporate radiative corrections (for details, see [12,20]), and we account for thermal Doppler broadening at 30 K.

When calculating $R_\beta(E)$, we sum over a final-state distribution (FSD) which is given by the probabilities ζ_j with which the daughter ion $^3\mathrm{He}T^+$ is left in a molecular (i.e., a rotational, vibrational, and electronic) state with excitation energy V_j. For this analysis, we first confirm the most recent theoretical FSD calculations [50,51] using new codes for solving the electronic and rovibrational problems within the Born-Oppenheimer approximation. We then refine the FSD by adopting a more efficient treatment of the rovibrational part and an update of other kinematics-related quantities, such as molecular masses, as well as recoil parameters (momenta and kinetic energy shifts). Most importantly, we treat all isotopologues (T_2, HT, and DT) in a consistent way with initial angular momenta distributions J_κ ($\kappa = 0, \ldots, 3$) at 30 K for the electronic bound states $n = 1, \ldots, 6$. The FSD includes higher excitation energies up to the continuum based on [50], but their contribution to our analysis interval $[E_0 - 40\ \mathrm{eV}]$ is at an overall level of 10^{-4} only. Accordingly, the FSD uncertainties in our narrow analysis interval of 40 eV below E_0 only contribute at the level of $0.02\ \mathrm{eV}^2$ to the total systematics budget on m_ν^2 (see Table I).

The response function $f_{\mathrm{calc}}(E - qU)$ used in the analysis is shown as the red curve in Fig. 2 (top). It corresponds to β-decay electrons born with energies close to E_0 and emitted isotropically up to θ_{max} in the source gas. Compared to the e-gun beam, they possess a different distribution of energy losses due to their broader range of pitch angles θ and the varying amount of source gas (ρd) they traverse. These processes are studied on the basis of gas dynamical simulations [52] which yield an approximately triangular-shaped longitudinal source profile.

After modeling the energy loss of β-decay electrons through the source by making use of $\rho d \cdot \sigma$ and $\varepsilon(\delta E)$, their subsequent propagation is tracked by the KASSIOPEIA simulation software [53]. It incorporates a detailed beam line model which takes account of the small radial inhomogeneities of B_{min} and qU at the analyzing plane. The full model provides the detailed shape of ΔE and the distribution of electron pitch angles up to θ_{max} from the parameters of the magnetic field triplet (B_{WGTS}, B_{min}, B_{max}).

The energy-independent part of $R_{\mathrm{calc}}(\langle qU \rangle)$, R_{bg}, comes from a fit of the spectrum $\mathrm{R}(\langle qU \rangle)$ over our 90 eV scan range. The fit value $R_{\mathrm{bg}} = (0.293 \pm 0.001)$ cps is largely constrained by the 5 HV set points above E_0 and agrees with data from independent background runs taken with an empty source before the tritium measurements.

The resulting model, $R_{\mathrm{calc}}(\langle qU \rangle)$, is then fitted to $R(\langle qU \rangle)$. To ensure that this proceeds without bias, we employ a twofold "blinding" scheme. The first blinding step leaves the data untouched, but a modification is applied during the building of the model $R_{\mathrm{calc}}(\langle qU \rangle)$. The FSD part describing rovibrational excitations of the electronic ground state is replaced with a Gaussian distribution with parameters not accessible to the analysis at first. As a result, fits with the blinded FSD do not reveal the unbiased value of m_ν^2. The "true" FSD is revealed only at the last step ("unblinding") after having fixed all model inputs and systematic uncertainties.

The second measure to mitigate biasing is to perform the full analysis, including parameter fitting, using Monte Carlo–based (MC) data sets first, before turning to the experimental data. For each experimental scan k, we generate a "MC twin," $R_{\mathrm{calc}}(\langle qU \rangle)_k$, from its averaged slow-control parameters to procure $R_\beta(E)_k$, $f_{\mathrm{calc}}(E - \langle qU \rangle)_k$, and $R_{\mathrm{bg},k}$. Analysis of MC twins allows us to verify the accuracy of our parameter inference by recovering the correct input MC values for m_ν^2. This approach is also used to assess statistical (σ_{stat}) and systematic (σ_{syst}) uncertainties and to compute our expected sensitivity.

In the following, we report on the results of two independent analyses with different strategies to propagate systematic uncertainties: the "Covariance Matrix" and the "MC propagation" approaches.

In the covariance method, we fit the experimental spectrum $R(\langle qU \rangle)$ with the model $R_{\mathrm{calc}}(\langle qU \rangle)$ by minimizing the standard χ^2 estimator. To propagate the systematic uncertainties, a covariance matrix is computed after performing $O(10^4)$ simulations of $R_{\mathrm{calc}}(\langle qU \rangle)$, while varying the relevant parameters for each calculation according to the likelihood given by their uncertainties [35,54,55]. The resulting systematic uncertainties agree with the values shown in Table I, which is based on the second approach. The sum of all matrices encodes the total uncertainties of $R_{\mathrm{calc}}(\langle qU \rangle)$ and their HV set point dependent correlations. The χ^2 estimator is then minimized to determine the four best-fit parameters, and the shape of χ^2 function is used to infer the uncertainties. The results of this fit are displayed in Fig. 3. We obtain a goodness-of-fit of $\chi^2 = 21.4$ for 23 d.o.f., corresponding to a p value of 0.56.

The MC-propagation approach is a hybrid Bayesian-frequentist method, adapted from Refs. [56–58]. We fit the experimental spectrum $R(\langle qU \rangle)$ with the model $R_{\mathrm{calc}}(\langle qU \rangle)$ by minimizing the negative Poisson-likelihood function. The goodness-of-fit of $-2 \ln \mathcal{L} = 23.3$ for 23 d.o.f. corresponds to a p value of 0.44. To propagate the systematic uncertainties, we repeat the fit 10^5 times, while varying the relevant parameters in each fit according to their uncertainties given in column 2 of Table I.

We report the 1σ width of the fit parameters as their systematic uncertainty in the third column of Table I. In order to simultaneously treat statistical and all systematic uncertainties, each of the 10^5 fits is performed on a statistically fluctuated MC copy of the true data set, leading to the distributions of m_ν^2 and E_0 shown in Fig. 4.

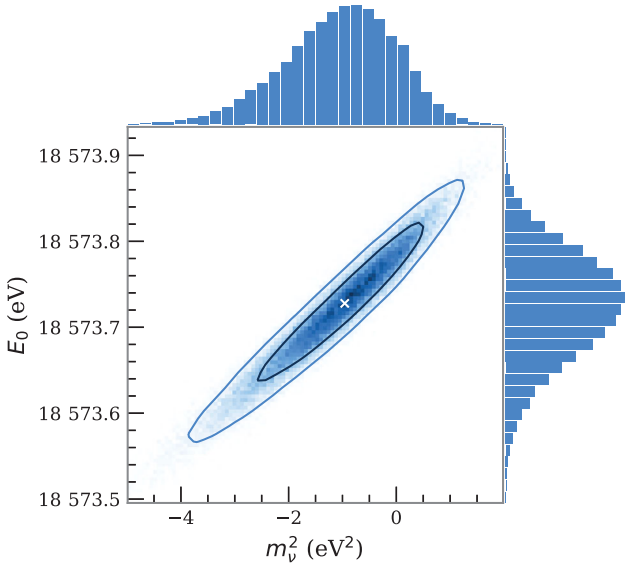

FIG. 4. Scatter plot of fit values for the mass square m_ν^2 and the effective β-decay end point E_0 together with 1σ (black) and 2σ (blue) error contours around the best fit point (cross). It follows from a large set of pseudoexperiments emulating our experimental data set and its statistical and systematical uncertainties.

The strong correlation (0.97) between the two parameters is an expected feature in kinematic studies of β decay [11,12]. The final-best fit is given by the mode of the fit-parameter distributions, and the 1σ total error is determined by integrating the distributions up to 16% from either side.

Results.—The two independent methods agree to within a few percent of the total uncertainty. As best fit value for the neutrino mass, we find $m_\nu^2 = (-1.0^{+0.9}_{-1.1})$ eV^2. This best fit result corresponds to a 1σ statistical fluctuation to negative values of m_ν^2 possessing a p value of 0.16.

The total uncertainty budget of m_ν^2 is largely dominated by σ_{stat} (0.97 eV^2) as compared to σ_{syst} (0.32 eV^2). As displayed in Table I, the dominant contributions to σ_{syst} are found to be the non-Poissonian background from radon and the uncertainty on the background slope, which is constrained from the wide-energy integral scans of the earlier "first tritium" data [35]. Uncertainties of the column density, energy-loss function, final-state distribution, and magnetic fields play a minor role in the budget of σ_{syst}. Likewise, the uncertainties induced via fluctuations of ε_T and HV parameters during a scan are negligibly small compared to σ_{stat}. The statistical (systematic) uncertainty of our first result on m_ν^2 is smaller by a factor of 2 (6) compared to the final results of Troitsk and Mainz [24,25].

The methods of Lokhov and Tkachov (LT) [59] and of Feldman and Cousins (FC) [60] are then used to calculate the upper limit on m_ν. Both procedures avoid empty confidence intervals for nonphysical negative best-fit estimates of m_ν^2. For this first result, we follow the LT method. For a statistical fluctuation into the nonphysical region the method returns a confidence belt that coincides with the experimental sensitivity and avoids a shrinking upper limit for more negative values of m_ν^2. Using the LT construction, we derive an upper limit of $m_\nu < 1.1$ eV (90% C.L.) as the central result of this Letter. By construction, it is identical to the expected sensitivity. For completeness, we also note the FC upper limits $m_\nu < 0.8(0.9)$ eV at 90% (95%) C.L.

For the effective end point, our two analysis methods both obtain the best-fit value $E_0 = (18\,573.7 \pm 0.1)$ eV (see Fig. 4). At this level of precision, a consistency check on the energy scale of KATRIN can be performed by comparing our experimental Q value for molecular tritium with that based on measurements of the ^{3}He-^{3}H atomic mass difference [61]. Our result for the Q value of (18575.2 ± 0.5) eV is obtained from our best-fit value for E_0 by adding the center-of-mass molecular recoil of T_2 (1.72 eV) [11], as well as the relative offset $(-0.2 \pm 0.5$ eV) of the source potential to the work function of the inner electrode. The calculated Q value from the ^{3}He-^{3}H atomic mass difference is (18575.72 ± 0.07) eV when accounting for the different binding energies and kinematic variables of atomic and molecular tritium [11]. The consistency of both Q values underlines the robustness of the energy scale in our scanning process of molecular tritium.

Conclusion and outlook.—The reported upper limit $m_\nu < 1.1$ eV (90% C.L.) improves upon previous results [24,25] by almost a factor of 2 after a measuring period of only four weeks while operating at reduced column density. It is based on a purely kinematic method. As such, it has implications for both particle physics and cosmology. For the former, it narrows down the allowed range of quasi-degenerate neutrino mass models by a direct method. For the latter, this model-independent limit can be used as laboratory-based input for studies of structure evolution in ΛCDM and other cosmological models.

Our result shows the potential of KATRIN to probe m_ν by a direct kinematic method. After 1000 days of data taking at nominal column density and further reductions of systematics and R_{bg}, we will reach a sensitivity of 0.2 eV (90% C.L.) on m_ν, augmented by searches for physics beyond the SM, such as for sterile neutrino admixtures with masses from the eV to the keV scale.

We acknowledge the support of the Helmholtz Association, Ministry for Education and Research BMBF (Grants No. 5A17PDA, No. 05A17PM3, No. 05A17PX3, No. 05A17VK2, and No. 05A17WO3), Helmholtz Alliance for Astroparticle Physics (HAP), Helmholtz Young Investigator Group (Grant No. VH-NG-1055), Max Planck Research Group (MaxPlanck@TUM), and Deutsche Forschungsgemeinschaft DFG (Research Training Groups Grants No. GRK 1694 and No. GRK 2149, and Graduate School Grant No. GSC 1085—KSETA) in Germany; Ministry of Education, Youth and Sport (Grants No. CANAM-LM2011019, and

No. LTT19005) in the Czech Republic; and the United States Department of Energy through Grants No. DE-FG02-97ER41020, No. DE-FG02-94ER40818, No. DE-SC0004036, No. DE-FG02-97ER41033, No. DE-FG02-97ER41041, No. DE-AC02-05CH11231, No. DE-SC0011091, and No. DE-SC0019304, and the National Energy Research Scientific Computing Center.

[*]Deceased.
[†]Corresponding author.
guido.drexlin@kit.edu
[‡]Corresponding author.
weinheimer@uni-muenster.de
[§]Formerly. K. Bokeloh (née Hugenberg)
[‖]Formerly. M. Kleesiek (né Haag)
[¶]Formerly. L. Kuckert (née Neumann)
[**]Formerly. L. I. Minter (née Bodine)
[††]Also at: Oak Ridge National Laboratory, Oak Ridge, Tennessee 37831, USA.

[1] Y. Fukuda *et al.* (Super-Kamiokande Collaboration), Evidence for Oscillation of Atmospheric Neutrinos, Phys. Rev. Lett. **81**, 1562 (1998).
[2] Q. R. Ahmad *et al.* (SNO Collaboration), Direct Evidence for Neutrino Flavor Transformation from Neutral-Current Interactions in the Sudbury Neutrino Observatory, Phys. Rev. Lett. **89**, 011301 (2002).
[3] I. Esteban, M. C. Gonzalez-Garcia, A. Hernandez-Cabezudo, M. Maltoni, and T. Schwetz, Global analysis of three-flavour neutrino oscillations: Synergies and tensions in the determination of $\theta_2 3$, $\delta_C P$, and the mass ordering, J. High Energy Phys. 01 (2019) 106.
[4] S. Hannestad, Primordial neutrinos, Annu. Rev. Nucl. Part. Sci. **56**, 137 (2006).
[5] J. Lesgourgues and S. Pastor, Neutrino cosmology and Planck, New J. Phys. **16**, 065002 (2014).
[6] A. Loureiro *et al.*, On The Upper Bound of Neutrino Masses from Combined Cosmological Observations and Particle Physics Experiments, Phys. Rev. Lett. **123**, 081301 (2019).
[7] S. F. King, A. Merle, S. Morisi, Y. Shimizu, and M. Tanimoto, Neutrino mass and mixing: From theory to experiment, New J. Phys. **16**, 045018 (2014).
[8] N. Aghanim *et al.* (Planck Collaboration), Planck 2018 results. VI. Cosmological parameters, arXiv:1807.06209v2.
[9] A. S. Barabash, Main features of detectors and isotopes to investigate double beta decay with increased sensitivity, Int. J. Mod. Phys. A **33**, 1843001 (2018).
[10] M. J. Dolinski, A. W. Poon, and W. Rodejohann, Neutrinoless double-beta decay: Status and prospects, Annu. Rev. Nucl. Part. Sci. **69**, 219 (2019).
[11] E. W. Otten and C. Weinheimer, Neutrino mass limit from tritium β decay, Rep. Prog. Phys. **71**, 086201 (2008).
[12] G. Drexlin, V. Hannen, S. Mertens, and C. Weinheimer, Current direct neutrino mass experiments, Adv. High Energy Phys. **2013**, 293986 (2013).
[13] L. Gastaldo *et al.*, The electron capture in ^{163}Ho experiment ECHo, Eur. Phys. J. Spec. Top. **226**, 1623 (2017).
[14] A. Nucciotti, The use of low temperature detectors for direct measurements of the mass of the electron neutrino, Adv. High Energy Phys. **2016**, 9153024 (2016).
[15] A. Ashtari Esfahani *et al.* (Project 8 Collaboration), Determining the neutrino mass with cyclotron radiation emission spectroscopy—Project 8, J. Phys. G **44**, 054004 (2017).
[16] M. Tanabashi *et al.* (Particle Data Group), Review of particle physics, Phys. Rev. D **98**, 030001 (2018).
[17] A. Osipowicz *et al.* (KATRIN Collaboration), KATRIN: A Next generation tritium beta decay experiment with sub-eV sensitivity for the electron neutrino mass. Letter of intent, arXiv:hep-ex/0109033.
[18] J. Angrik *et al.* (KATRIN Collaboration), Katrin design report, FZKA Scientific Report No. 7090, 1 (2005), https://www.katrin.kit.edu/publikationen/DesignReport2004-12Jan2005.pdf.
[19] M. Arenz *et al.* (KATRIN Collaboration), First transmission of electrons and ions through the KATRIN beamline, J. Instrum. **13**, P04020 (2018).
[20] M. Kleesiek *et al.*, β-decay spectrum, response function and statistical model for neutrino mass measurements with the KATRIN experiment, Eur. Phys. J. C **79**, 204 (2019).
[21] R. G. H. Robertson, T. J. Bowles, G. J. Stephenson, D. L. Wark, J. F. Wilkerson, and D. A. Knapp, Limit on $\bar{\nu}_e$ Mass from Observation of the β Decay of Molecular Tritium, Phys. Rev. Lett. **67**, 957 (1991).
[22] V. M. Lobashev and P. E. Spivak, A method for measuring the anti-electron-neutrino rest mass, Nucl. Instrum. Methods Phys. Res., Sect. A **240**, 305 (1985).
[23] A. Picard, H. Backe, H. Barth, J. Bonn, B. Degen, T. Edling, R. Haid, A. Hermanni, P. Leiderer, T. Loeken, A. Molz, R. B. Moore, A. Osipowicz, E. W. Otten, M. Przyrembel, M. Schrader, M. Steininger, and C. Weinheimer, A solenoid retarding spectrometer with high resolution and transmission for keV electrons, Nucl. Instrum. Methods Phys. Res., Sect. B **63**, 345 (1992).
[24] C. Kraus, B. Bornschein, L. Bornschein, J. Bonn, B. Flatt, A. Kovalik, B. Ostrick, E. W. Otten, J. P. Schall, T. Thümmler, and C. Weinheimer, Final results from phase II of the Mainz neutrino mass search in tritium β decay, Eur. Phys. J. C **40**, 447 (2005).
[25] V. N. Aseev, A. I. Belesev, A. I. Berlev, E. V. Geraskin, A. A. Golubev, N. A. Likhovid, V. M. Lobashev, A. A. Nozik, V. S. Pantuev, V. I. Parfenov, A. K. Skasyrskaya, F. V. Tkachov, and S. V. Zadorozhny, Upper limit on the electron antineutrino mass from the Troitsk experiment, Phys. Rev. D **84**, 112003 (2011).
[26] F. Priester, M. Sturm, and B. Bornschein, Commissioning and detailed results of KATRIN inner loop tritium processing system at Tritium Laboratory Karlsruhe, Vacuum **116**, 42 (2015).
[27] M. Arenz *et al.* (KATRIN Collaboration), The KATRIN superconducting magnets: Overview and first performance results, J. Instrum. **13**, T08005 (2018).
[28] F. M. Fränkle *et al.*, Penning discharge in the KATRIN pre-spectrometer, J. Instrum. **9**, P07028 (2014).
[29] M. Beck *et al.*, Effect of a sweeping conductive wire on electrons stored in the Penning trap between the KATRIN spectrometers, Eur. Phys. J. A **44**, 499 (2010).

[30] M. Arenz *et al.* (KATRIN Collaboration), Commissioning of the vacuum system of the KATRIN Main Spectrometer, J. Instrum. **11**, P04011 (2016).

[31] M. Erhard *et al.*, Technical design and commissioning of the KATRIN large-volume air coil system, J. Instrum. **13**, P02003 (2018).

[32] J. F. Amsbaugh *et al.*, Focal-plane detector system for the KATRIN experiment, Nucl. Instrum. Methods Phys. Res., Sect. A **778**, 40 (2015).

[33] M. Arenz *et al.*, Calibration of high voltages at the ppm level by the difference of $^{83\,m}$Kr conversion electron lines at the KATRIN experiment, Eur. Phys. J. C **78**, 368 (2018).

[34] S. Grohmann, T. Bode, M. Hötzel, H. Schön, M. Süsser, and T. Wahl, The thermal behaviour of the tritium source in KATRIN, Cryogenics **55–56**, 5 (2013).

[35] M. Aker *et al.* (KATRIN Collaboration), First operation of the KATRIN experiment with tritium, arXiv:1909.06069v1.

[36] J. W. Liu, Total cross sections for high-energy electron scattering by h_2 ($^1\Sigma_g^+$), n_2 ($^1\Sigma_g^+$), and o_2 ($^3\Sigma_g^-$), Phys. Rev. A **35**, 591 (1987).

[37] J. Behrens *et al.*, A pulsed, mono-energetic and angular-selective UV photo-electron source for the commissioning of the KATRIN experiment, Eur. Phys. J. C **77**, 410 (2017).

[38] J. Bonn, L. Bornschein, B. Degen, E. Otten, and C. Weinheimer, A high resolution electrostatic time-of-flight spectrometer with adiabatic magnetic collimation, Nucl. Instrum. Methods Phys. Res., Sect. A **421**, 256 (1999).

[39] F. M. Fraenkle (KATRIN collaboration), Background processes in the KATRIN main spectrometer, J. Phys. **888**, 012070 (2017).

[40] K. Altenmüller *et al.* (KATRIN Collaboration), Muon-induced background in the KATRIN main spectrometer, Astropart. Phys. **108**, 40 (2019).

[41] K. Altenmüller *et al.* (KATRIN Collaboration), Gamma-induced background in the KATRIN main spectrometer, Eur. Phys. J. C **79**, 807 (2019).

[42] N. Trost, Modeling and measurement of Rydberg-state mediated background at the KATRIN Main Spectrometer, Ph.D. thesis, Karlsruhe Institute of Technology, 2018.

[43] F. M. Fränkle, L. Bornschein, G. Drexlin, F. Glück, S. Görhardt, W. Käfer, S. Mertens, N. Wandkowsky, and J. Wolf, Radon induced background processes in the KATRIN pre-spectrometer, Astropart. Phys. **35**, 128 (2011).

[44] S. Görhardt *et al.*, Impact of a cryogenic baffle system on the suppression of radon-induced background in the KATRIN Pre-Spectrometer, J. Instrum. **13**, T10004 (2018).

[45] M. Schlösser, H. Seitz, S. Rupp, P. Herwig, C. G. Alecu, M. Sturm, and B. Bornschein, In-line calibration of raman systems for analysis of gas mixtures of hydrogen isotopologues with sub-percent accuracy, Anal. Chem. **85**, 2739 (2013).

[46] A. F. Nastoyashchii, N. A. Titov, I. N. Morozov, F. Glück, and E. W. Otten, Effects of plasma phenomena on neutrino mass measurements process using a gaseous tritium β-source, Fusion Sci. Technol. **48**, 743 (2005).

[47] D. Vénos, J. Sentkerestiová, O. Dragoun, M. Slezák, M. Ryšavý, and A. špalek, Properties of $^{83\,m}$Kr conversion electrons and their use in the KATRIN experiment, J. Instrum. **13**, T02012 (2018).

[48] T. Thummler, R. Marx, and C. Weinheimer, Precision high voltage divider for the KATRIN experiment, New J. Phys. **11**, 103007 (2009).

[49] M. Babutzka *et al.*, Monitoring of the operating parameters of the KATRIN Windowless Gaseous Tritium Source, New J. Phys. **14**, 103046 (2012).

[50] A. Saenz, S. Jonsell, and P. Froelich, Improved Molecular Final-State Distribution of HeT^+ for the β-Decay Process of T_2, Phys. Rev. Lett. **84**, 242 (2000).

[51] N. Doss, J. Tennyson, A. Saenz, and S. Jonsell, Molecular effects in investigations of tritium molecule β decay end-point experiments, Phys. Rev. C **73**, 025502 (2006).

[52] L. Kuckert, F. Heizmann, G. Drexlin, F. Glück, M. Hötzel, M. Kleesiek, F. Sharipov, and K. Valerius, Modelling of gas dynamical properties of the KATRIN tritium source and implications for the neutrino mass measurement, Vacuum **158**, 195 (2018).

[53] D. Furse *et al.*, Kassiopeia: A modern, extensible C++ particle tracking package, New J. Phys. **19**, 053012 (2017).

[54] R. J. Barlow, *Statistics: A Guide to the Use of Statistical Methods in the Physical Sciences*, Manchester physics series (Wiley, Chichester, 1989).

[55] G. D'Agostini, On the use of the covariance matrix to fit correlated data, Nucl. Instrum. Methods Phys. Res., Sect. A **346**, 306 (1994).

[56] G. Cowan, K. Cranmer, E. Gross, and O. Vitells, Asymptotic formulae for likelihood-based tests of new physics, Eur. Phys. J. C **71**, 1554 (2011); Erratum, Eur. Phys. J. C **73**, 2501(E) (2013).

[57] R. D. Cousins and V. L. Highland, Incorporating systematic uncertainties into an upper limit, Nucl. Instrum. Methods Phys. Res., Sect. A **320**, 331 (1992).

[58] P. Harris and M. G. Cox, On a Monte Carlo method for measurement uncertainty evaluation and its implementation, Metrologia **51**, S176 (2014).

[59] A. V. Lokhov and F. V. Tkachov, Confidence intervals with a priori parameter bounds, Phys. Part. Nucl. **46**, 347 (2015).

[60] G. J. Feldman and R. D. Cousins, A Unified approach to the classical statistical analysis of small signals, Phys. Rev. D **57**, 3873 (1998).

[61] E. G. Myers, A. Wagner, H. Kracke, and B. A. Wesson, Atomic Masses of Tritium and Helium-3, Phys. Rev. Lett. **114**, 013003 (2015).